Nanoscale

ROYAL SOCIETY OF CHEMISTRY

PAPER

View Article Online
View Journal | View Issue

Cite this: *Nanoscale*, 2024, **16**, 6488

Solid-waste-recycled CuO/C_3N_4 S-scheme heterojunctions for efficient photocatalytic antibiotic degradation†

Jiawen Liu,[a] Jiahui Lin,[a] Kai Yi,[a] Fangyan Liu,[b] Feng Gao,[a] Mengye Wang *[a] and Feng Huang [a,c]

With the increasing severity of antibiotic pollution, the development of effective green photocatalysts for the degradation of organic pollutants in water has attracted extensive attention. Herein, we have prepared CuO/C_3N_4 S-scheme heterogeneous photocatalysts *via* recycling Cu resources from Cu-containing electroplating sludges. By mediating the acid leaching process, copper in electroplating sludges was dissolved selectively, while other metal species were retained in the residues. The CuO/C_3N_4 S-scheme heterojunction not only effectively suppressed the recombination of photogenerated charge carriers of C_3N_4, but also preserved the strong reducing electrons of C_3N_4 and the strong oxidizing holes of CuO, retaining the outstanding redox ability of CuO/C_3N_4. Therefore, CuO/C_3N_4 photocatalysts exhibited good catalytic performance in the degradation of tetracycline (over 95% in 2 h). In addition, CuO/C_3N_4 S-scheme heterojunctions achieved a high mineralization rate (45% in 2 hours), thus reducing secondary pollution during the degradation. This work provides a reliable direction for designing novel S-scheme heterojunction photocatalytic materials by using metal sources in solid waste.

Received 15th December 2023,
Accepted 29th February 2024

DOI: 10.1039/d3nr06410g

rsc.li/nanoscale

[a]*State Key Laboratory of Optoelectronic Materials and Technologies, School of Materials, Sun Yat-Sen University, Guangzhou, 510275, China. E-mail: wangmengye@mail.sysu.edu.cn*

[b]*State Key Laboratory of Optoelectronic Materials and Technologies, Guangdong Province Key Laboratory of Display Material and Technology, School of Electronics and Information Technology, Sun Yat-Sen University, Guangzhou, 510275, China*

[c]*Ganjiang Innovation Academy, Chinese Academy of Sciences, Ganzhou, 341000, China*

†Electronic supplementary information (ESI) available. See DOI: https://doi.org/10.1039/d3nr06410g

Mengye Wang

Mengye Wang is an Associate Professor in the School of Materials at Sun Yat-Sen University. She received her PhD in Physical Chemistry from Xiamen University. She is the board member of Materials Horizons, Journal of Materials Chemistry A, Materials Advances, Nano Research, Nano Research Energy, Journal of Synthetic Crystals, and Rare Metals and Cleaner Materials. Her research interests include advanced materials for environmental and energy-related applications, such as photocatalysis, piezocatalysis and electrocatalysis.

1. Introduction

Among the critical resources essential for human survival, water reservoirs have endured substantial pollution, further exacerbating the crisis.[1–5] The excessive and improper utilization of antibiotics has led to pervasive contamination of water resources, profoundly threatening the ecological balance.[6,7] In response to this urgent issue, diverse strategies have been developed, such as photocatalytic degradation,[8] electrochemical degradation[9–11] and biodegradation.[12] Notably, photocatalytic degradation has been extensively investigated due to its ability to harness renewable solar energy, aligning with sustainable and environmentally friendly practices.[13–15] Photocatalysis holds immense promise in tackling the challenge posed by antibiotic pollution in water.[16]

As the key to photocatalytic degradation, the issue of how to improve the separation efficiency of photogenerated carriers needs to be urgently resolved.[17–22] To solve this problem, it is a common method to construct heterojunctions. However, in the conventional type II heterojunction structure, the carrier separation efficiency is improved at the expense of the redox capacity of the catalyst.[23] By forming an internal electric field between an oxidation catalyst and a reduction catalyst, the S-scheme heterojunction can not only ensure the effective carrier separation of both catalysts, but also improve their redox capability.[24–26] Among the common photocatalysts, C_3N_4 has garnered significant attention due to its narrow band gap,

suitability for visible light absorption, facile synthesis, excellent thermal stability, and robust acid and alkaline resistance.[27–32] Although the narrow band gap of C_3N_4 brings a good visible light absorption capacity, it restricts the redox capacity of C_3N_4. In addition, pure-phase C_3N_4 also exhibits drawbacks in photocatalysis, such as high carrier recombination rate.[33,34] By combining C_3N_4 with CuO with its more positive valence band to form an S-scheme heterojunction, the carrier separation efficiency and redox ability of C_3N_4 can be intensively improved.

As one of the indispensable metals in our daily life, copper products are widely used in all walks of life. However, the extensive use of copper products has resulted in large amounts of copper-containing solid waste.[35] Considering prevailing resource scarcity, these solid waste materials represent misallocated reserves of accessible metal resources.[36,37] In our work, a simple approach was employed to extract copper from solid waste through acid leaching and integrate it with C_3N_4 to fabricate CuO/C_3N_4 composite heterojunction materials. Considering that both CuO and C_3N_4 are n-type semiconductors with significant difference in electronic band positions, a novel S-scheme heterojunction could be constructed. The formation of the S-scheme heterojunction was verified through the characterization of Mott–Schottky curves and band structures. Due to the electrons in C_3N_4 at the high Fermi level drifting to CuO at the low Fermi level, the C_3N_4 interface became positively charged and the CuO interface became negatively charged, creating an internal electric field directed from CuO to C_3N_4. At the same time, the energy bands at the C_3N_4 and CuO interfaces were also bent upward and downward, respectively. This band bending and the formation of the internal electric field effectively inhibited carrier recombination and increased carrier lifetime from 1.32 ns to 4 ns. In addition, strong reducing electrons and oxidizing holes were retained in the conduction band of C_3N_4 and the valence band of CuO, respectively, which preserved the strong redox ability of CuO/C_3N_4. After a photocatalytic reaction for 2 h, the degradation rate of tetracycline exceeded 95%, and its mineralization rate approached 50%. These results confirmed the significant photocatalytic performance of the CuO/C_3N_4 materials.

2. Experimental

2.1 Chemical reagents

The following reagents were directly used without further purification: sulfuric acid (H_2SO_4, Guangzhou Chemical Reagent Factory), melamine (Macklin, 98%), cyanuric acid (Macklin, 99%), potassium hydroxide (KCl, 99.8%, Macklin), ethanol (99.8%, Macklin) and Nafion (5%, DuPont). All experiments used deionized (DI) water.

2.2 Synthesis

Pretreatment of the copper-bearing solid waste. The solid waste was supplied by Shenzhen Suntak Circuit Technology Co., Ltd. Firstly, the copper-bearing solid waste was dried at 70 °C for 24 h and broken into powder. Then, the powder was soaked and dissolved in 1 M H_2SO_4 solution followed by stirring for 3 h. The Cu leachate was obtained after filtration.

Synthesis of CuO/C_3N_4. The typical process of preparing CuO/C_3N_4 catalyst with different proportions was as follows: 2 g of melamine and 2 g of cyanuric acid were added into a mixed solution of 2 ml of Cu leachate and 28 ml of water, and the mixture stirred for 2 hours after half an hour of ultrasound treatment. The resulting suspension was centrifuged at 11 000 rpm for 5 minutes; the sediment obtained was composed of a macromolecular polymer containing copper ions. Different proportions of CuO/C_3N_4 composites were obtained by calcining 4 g, 3 g, and 2 g of the precipitate in a covered crucible at 550 °C in a muffle furnace for 2 hours, which were named as CuO/C_3N_4-1, CuO/C_3N_4-2 and CuO/C_3N_4-3, respectively.

Synthesis of CuO. 2 g of melamine and 2 g of cyanuric acid were added into the mixed solution of 2 ml of Cu leachate and 28 ml of water, and stirred for 2 h after half an hour of ultrasonication. The resulting suspension was centrifuged at 11 000 rpm for 5 minutes and the sediment composed of a macromolecular polymer containing copper ions was obtained. The dried macromolecular polymer was calcined in an open crucible at 550 °C in a muffle furnace for 2 h to obtain the CuO catalyst.

Synthesis of pure C_3N_4. The other procedures of the synthesis method remained unchanged, except that the Cu leachate was replaced by DI water.

2.3 Characterization studies

Scanning electron microscopy (SEM) images were taken using a field emission scanning electron microscope (FESEM) on a ZEISS Merlin (Zeiss) spectrophotometer to observe the morphology. Powder X-ray diffraction (XRD) patterns were recorded using a Bruker D8-Advance X-ray diffractometer with Cu Kα radiation (λ = 0.154 nm) at 40 kV and 40 mA. Transmission electron microscopy (TEM) and high-resolution transmission electron microscopy (HRTEM) images of the nanostructures were recorded on an electron microscope (FEI-TALOS-F200X) operating at an accelerating voltage of 200 kV. Diffuse reflectance UV-vis spectra (DRS) were recorded on a SHIMADZU UV-2600i spectrophotometer. Fourier transform infrared (FTIR) spectroscopy was performed on a Bruker INVENIO R within the range from 4000 to 400 cm^{-1}. X-ray photoelectron spectroscopy (XPS) was monitored on a Thermo Scientific K-Alpha photoelectron spectrometer. The steady-state and time resolution photoluminescence (PL) spectra were used to analyze photogenerated electron–hole separation efficiency. Electrochemical testing was carried out by using an electrochemical analyzer (CHI660e).

2.4 Photocatalytic degradation measurements

Photocatalytic tetracycline degradation was carried out in a quartz reactor equipped with a cooling water circulation device. Typically, 20 mg of the catalyst were dispersed into 100 ml of 30 mg L^{-1} tetracycline aqueous solution at room

temperature. A 300 W Xe lamp was used as a visible light source, placed 10 cm above the reactor. At first, the suspension was stirred in the dark for 30 min to achieve the equilibrium of absorption and desorption. Then, 5 ml of the sample was extracted under light every half hour to record the ultraviolet absorption spectrum to determine the tetracycline concentration.

2.5 Photoelectrochemical measurements

An electrochemical workstation (CHI660e) was used to measure the photocurrent responses and electrochemical impedance spectra (EIS). All the tests were carried out by using a three-electrode system, including a reference Ag/AgCl electrode, a counter electrode of Pt foil, and a working electrode of ITO glass-supported photocatalyst. To prepare the working electrode, the ITO glass was cleaned by ultrasonic cleaning with acetone, ethanol and DI water. Then, 100 μl of photocatalyst ink was dropped onto the ITO glass and dried under an infrared lamp. The ink was prepared by ultrasonically mixing 10 mg of photocatalyst and 50 μl of Nafion in a solution of 1560 μl of DI water and 390 μl of ethanol. 0.1 M K_2SO_4 solution was used as the electrolyte. The *I*–*t* curve was recorded under illumination (300 W xenon lamp). EIS measurements were carried out at open circuit voltage (OCP). The Mott–Schottky data were collected at 1 kHz. The carrier concentration was estimated according to the Mott–Schottky equation:

$$C_{SC}^{-2} = \frac{2}{\varepsilon\varepsilon_0 e N_D}\left(E - E_{fb} - \frac{kT}{e}\right)$$

where C_{SC} is the capacitance derived from the electrochemical impedance obtained at each potential with 1 kHz frequency in the dark, ε is the dielectric constant, ε_0 is the permittivity in a vacuum, and N_D is the donor density.

3. Results and discussion

Fig. 1a shows the XRD pattern of the raw sludge. The main phases contain $CaCO_3$, $BaSO_4$, $Cu_4Fe_5S_8$, $BaCuO_{2.36}$ and SiO_2. X-ray fluorescence (XRF) was used to analyze the content of each element in the sludge. The main metals in the raw sludge were Cu, Fe and Ca, which were 50.8%, 16.4% and 16.4%, respectively (Fig. 1b). Fig. 1c depicts the fabrication process of the CuO/C_3N_4 catalysts. The plating sludge containing copper was first dried and broken, and then soaked in the acid solution. The metal species were dissolved by acid leaching, and then Fe^{3+} and Ca^{2+} were precipitated by controlling the amount of acid and anions added. Meanwhile, the copper ions were retained in the leachate. Melamine and cyanuric acid were added to the Cu leachate solution. During the stirring process, melamine and cyanuric acid were connected through hydrogen bonds (N–H···N/O) to form macromolecular polymers. Copper ions were anchored on the surface of the polymer due to pH changes. The obtained suspension was subsequently subjected to centrifugation and drying processes,

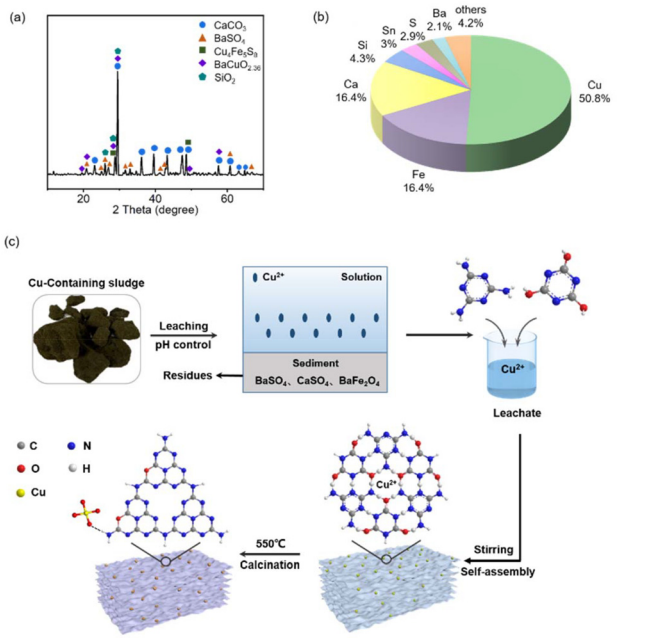

Fig. 1 (a) XRD pattern of the sludge. (b) Pie chart of the elemental distribution of the sludge. (c) Schematic illustration of the synthetic process of CuO/C_3N_4.

yielding macromolecular precursors containing copper species. Subsequently, the macromolecular polymers were calcined at 550 °C, leading to the formation of CuO/C_3N_4 catalysts. The specific experimental procedures can be found in the ESI.† We carried out an ICP test on the Cu^{2+} concentration in the solid waste leachate solution and the solution after being treated. The Cu^{2+} concentrations were 14 255.6 mg L^{-1} and 39.7 mg L^{-1}, respectively, indicating that the copper ions in the waste were almost completely adsorbed and had a very good utilization rate. SEM images in Fig. S2† depict the morphologies of different samples, including pure C_3N_4, CuO/C_3N_4-1, CuO/C_3N_4-2, and CuO/C_3N_4-3. The lamellar structure of C_3N_4 without the addition of copper extract was observed and is shown in Fig. S2a.† This two-dimensional sheet structure effectively enhanced the exposure of C_3N_4 active sites and utilization of visible light. Meanwhile, the 2D sheet structure also greatly shortens the carrier mobility path from the bulk phase to the surface and reduces the carrier recombination efficiency. Upon the introduction of the copper-containing leachate, the flake morphology of the catalysts remained unchanged, as revealed in Fig. S2b–d.† Nanoparticles were observed on the surface of the sheet structure of CuO/C_3N_4, which were likely copper oxide nanoclusters (Fig. S2d†).

To investigate the morphology of copper oxide and C_3N_4, further characterization of CuO/C_3N_4-2 was conducted using transmission electron microscopy (TEM). TEM images provided direct visualization of the two-dimensional nanosheet structure of C_3N_4 (Fig. 2a). In Fig. 2b, the lattice spacing values of 0.25 nm and 0.33 nm can be observed, belonging to the (111) crystal plane of CuO and the (002) crystal plane of C_3N_4,

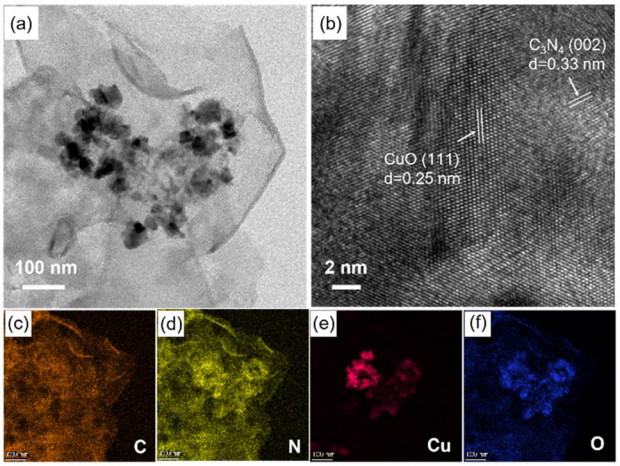

Fig. 2 (a) TEM image and (b) HRTEM image of CuO/C_3N_4-2. EDS elemental distribution mappings of (c) C, (d) N, (e) Cu and (f) O of CuO/C_3N_4-2.

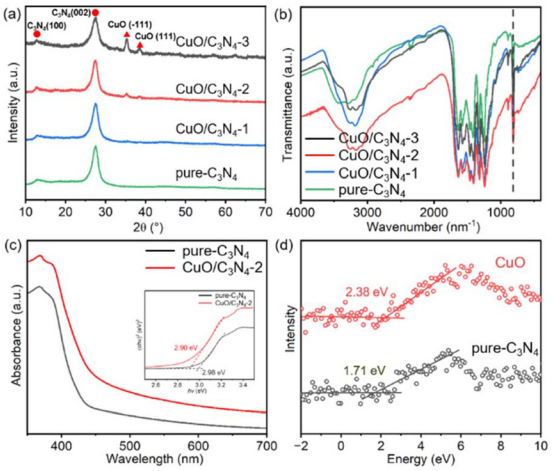

Fig. 3 (a) XRD patterns and (b) FTIR spectra of pure C_3N_4, CuO/C_3N_4-1, CuO/C_3N_4-2 and CuO/C_3N_4-3. (c) UV/Vis absorption spectra and the corresponding Tauc plots of pure C_3N_4 and CuO/C_3N_4-2. (d) XPS valence band energy plots of pure C_3N_4 and CuO.

respectively. This confirmed that the copper species were loaded onto C_3N_4 in the form of copper oxide after the calcination process and formed a heterogeneous interface. Cu and O elements were concentrated within the particle clusters, while C and N elements were uniformly distributed throughout the nanosheet structure. In Fig. 2f, it was observed that oxygen element also existed in the C_3N_4 sheet area. Considering that the macromolecular precursor was calcined under an air atmosphere, oxygen element was inevitably doped into the C_3N_4 lattice. Some studies have shown that oxygen doping could effectively regulate the electron state density and band structure of C_3N_4 and improve the catalytic efficiency.[38,39] This spatial distribution of elements provided additional evidence supporting the presence of CuO in the form of clusters on the surface of the C_3N_4 sheet.

In order to further explore the composition and phase structure of the as-synthesized samples, X-ray diffraction (XRD) patterns and Fourier transform infrared (FTIR) spectroscopy measurements were conducted. Pure C_3N_4 exhibited diffraction peaks at 12.8° and 27.5°, agreeing well with the (100) and (002) crystal planes of C_3N_4, respectively (Fig. 3a). Different proportions of CuO/C_3N_4 catalysts were prepared by changing the calcination amount of the macromolecular polymer precursors. From CuO/C_3N_4-1 to CuO/C_3N_4-3, the increasing intensity of peaks at 35.2° and 38.6° attributed to the (1−11) and (111) crystal planes of CuO, respectively, indicated that the content of CuO increased gradually. In Fig. 3b, IR signals at 815 cm^{-1}, 1150–1700 cm^{-1}, and 3000–3400 cm^{-1} were attributed to the structural bending of tri-*s*-triazine units, stretching vibration modes of C–N heterocycles and N–H stretching of the amino groups, respectively (Fig. 3b). Compared with pure C_3N_4, CuO/C_3N_4 showed no obvious change, indicating that the structure of C_3N_4 remained unchanged despite the modification of CuO.

The absorption capacity of visible light plays a crucial role in the photocatalytic performance of a photocatalytic material. To investigate the influence of copper oxide on the absorption capacity of C_3N_4, UV-vis absorption spectra were recorded. Compared with pure C_3N_4, CuO/C_3N_4-2 demonstrated a noticeable red shift in the absorption edge after the introduction of CuO. This observation indicated that the formation of a CuO/C_3N_4 heterojunction effectively broadened the wavelength range of light utilized by the catalyst. Moreover, the absorption intensity of the catalyst in the visible range was significantly enhanced in comparison with pure C_3N_4. This finding confirmed that the introduction of CuO contributed to the improvement of photon utilization efficiency of C_3N_4 during the photocatalytic process, leading to an enhanced overall photocatalytic performance of C_3N_4. By employing the Kubelka–Munk equation, the band gaps of pure C_3N_4 and CuO/C_3N_4-2 catalysts were calculated to be 2.98 eV and 2.90 eV, respectively. CuO loading thus reduced the band gap of C_3N_4 by approximately 0.08 eV. Moreover, the VB-XPS spectra of C_3N_4 and CuO are shown in Fig. 3d. These suggested that the VB was 2.38 eV and 1.71 eV for CuO and C_3N_4, respectively.

To investigate the chemical states of pure C_3N_4 and CuO/C_3N_4-2, X-ray photoelectron spectroscopy (XPS) was employed. Compared with pure C_3N_4, CuO/C_3N_4-2 exhibited additional binding energy peaks around 940 eV (Fig. 4a), which can be attributed to the presence of copper. High-resolution Cu2p XPS spectra of CuO/C_3N_4-2 are shown in Fig. 4b. The peaks at 951.8 eV and 932.0 eV were assigned to $Cu^{2+}2p_{1/2}$ and $Cu^{2+}2p_{3/2}$, respectively. The apparent satellite peaks at 961.7 eV and 941.9 eV in Fig. 4b indicate that the copper species was copper oxide rather than elemental copper or cuprous oxide. The high-resolution XPS spectra of N1s reveal peaks at 397.5 eV, 398.9 eV, and 400.1 eV, corresponding to nitrogen bonded in C–N=C in sp^2 hybridization, the N–C_3 bond in sp^3 hybridization, and the amino C–N–H bond in sp^3 hybridization, respectively (Fig. 4c). The ratio of sp^2 hybridized nitrogen to sp^3 hybridized nitrogen was calculated for the C_3N_4 and CuO/

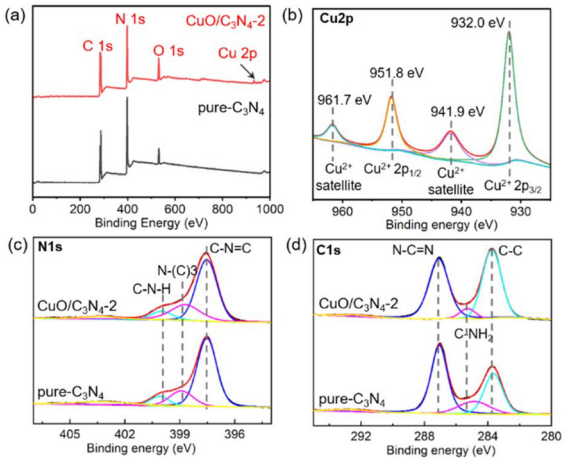

Fig. 4 (a) XPS survey spectra of pure C_3N_4 and CuO/C_3N_4-2. (b) High-resolution Cu2p XPS spectra of CuO/C_3N_4-2. High-resolution XPS spectra of (c) N1s and (d) C1s of pure C_3N_4 and CuO/C_3N_4-2.

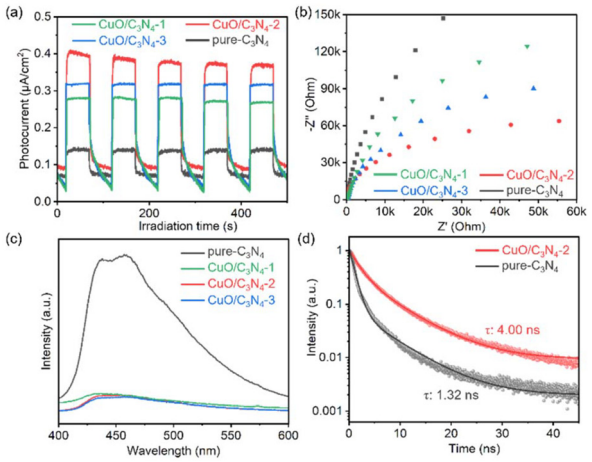

Fig. 5 (a) Photocurrent responses, (b) EIS spectra and (c) PL spectra of pure C_3N_4, CuO/C_3N_4-2, CuO/C_3N_4-2 and CuO/C_3N_4-3. (d) TRPL spectra of pure C_3N_4 and CuO/C_3N_4-2.

C_3N_4 samples, and it was 2.45 and 1.53, respectively. These findings suggested that the incorporation of copper species partly occupied the position of sp^2-hybridized nitrogen of C_3N_4, leading to a decrease in the content of sp^2-hybridized nitrogen. Additionally, the N/C atom ratio decreased from 0.75 to 0.6 upon the modification of copper oxide, indicating the emergence of nitrogen vacancies in the sp^2 hybrid nitrogen sites.

Fig. 4d displays the high-resolution XPS spectra of C1s. The peaks at 283.8 eV, 285.1 eV, and 287.1 eV were in agreement with graphitized carbon, the C–NH_2 bond, and sp^2 hybrid carbon, respectively. In comparison with C_3N_4, the proportion and position of carbon atoms connected to the amino group in CuO/C_3N_4 samples were significantly changed, indicating a strong interaction between copper oxide and C–NH_2. The ratio of sp^2 hybrid carbon to sp^3 hybrid carbon decreased from 1.61 to 1.03, which aligned with the change trend observed in the N/C atom ratio. This further confirmed the influence of copper oxide loading on the chemical environment of carbon and nitrogen elements of C_3N_4. Moreover, the presence of C–N=C structures in the N1s spectra and N–C=N structures in the C1s spectra demonstrated the existence of the tri-*s*-triazine ring structure in the sample.

To evaluate photogenerated carrier separation and transmission efficiency of pure C_3N_4 and CuO/C_3N_4, photocurrent measurements, electrochemical impedance spectroscopy (EIS), steady-state photoluminescence (PL) spectroscopy and time-resolved photoluminescence (TRPL) spectroscopy were conducted, as depicted in Fig. 5. The photocurrent generated by CuO/C_3N_4-2 (about 0.4 μA cm^{-2}) under xenon lamp illumination was 2.6 times greater than that of pure C_3N_4 (about 0.15 μA cm^{-2}, Fig. 5a). The photocurrent generated by CuO/C_3N_4-1 and CuO/C_3N_4-3 under the same xenon lamp was 0.28 μA cm^{-2} and 0.32 μA cm^{-2}, respectively. These results indicated that the introduction of CuO significantly enhanced the separation efficiency of photogenerated electrons and holes. The EIS spectra showed that the electrochemical impedance of CuO/C_3N_4-2, CuO/C_3N_4-3, CuO/C_3N_4-1 and pure C_3N_4 increased gradually (Fig. 5b). This suggested that the charge transfer ability at the interface between CuO/C_3N_4 and solution was substantially higher than that between pure C_3N_4 and solution, ultimately improving the photocatalytic efficiency. The fluorescence intensity of CuO/C_3N_4 was considerably lower than that of pure C_3N_4 (Fig. 5c). This indicated that the introduction of CuO effectively suppressed the recombination of photogenerated electrons and holes, leading to enhanced visible light utilization efficiency. By employing double exponential function fitting, the average lifetimes of pure C_3N_4 and CuO/C_3N_4-2 were calculated to be 1.32 ns and 4.00 ns, respectively. The average lifetime of CuO/C_3N_4-2 was approximately three times greater than that of pure C_3N_4, indicating that CuO decoration significantly decreased the recombination rate of photo-induced charge carriers.

To investigate the effect of CuO modification on the photocatalytic performance of C_3N_4, tetracycline (TC) was utilized as the target pollutant for degradation under xenon lamp irradiation. Tetracycline has caused significant environmental harm due to its widespread misuse. For comparison, the same degradation tests were performed with commercial CuO. The degradation experiments were performed using a 30 mg L^{-1} tetracycline solution with 20 mg of catalysts under xenon lamp illumination, preceded by a 30-minute adsorption test in the dark. The results demonstrated that the degradation rate of TC can exceed 95% within 2 hours using CuO/C_3N_4 as the catalyst, whereas the degradation rates of pure C_3N_4 and CuO were only around 50% (Fig. 6a). This tremendous improvement in degradation efficiency using CuO/C_3N_4 as the catalyst was primarily attributed to the introduction of copper oxide. The presence of copper oxide enhanced carrier separation efficiency, increased visible light utilization, and reduced carrier recombination rates, thereby facilitating the improved photocatalytic efficiency. In Fig. S3,† it is shown that the degradation rate of the sample was over 90% after five cycles. This result indicated that our samples have good stability under catalytic reactions.

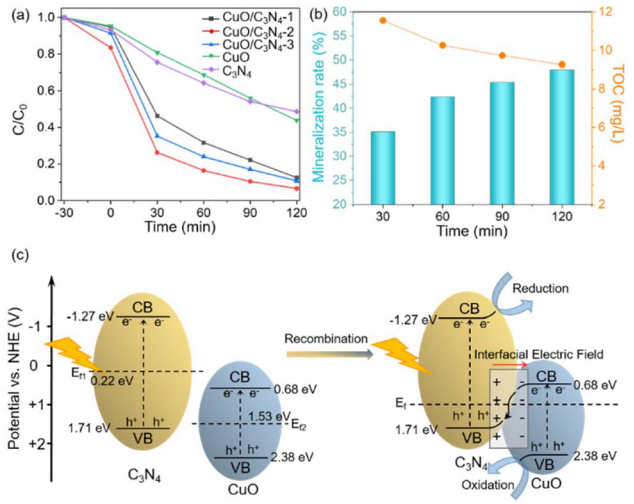

Fig. 6 (a) Photocatalytic performance of CuO, pure C_3N_4, CuO/C_3N_4-1, CuO/C_3N_4-2 and CuO/C_3N_4-3 for the removal of TC. (b) Mineralization rate and TOC removal efficiency of TC over CuO/C_3N_4-2. (c) Photocatalytic mechanism of CuO/C_3N_4-2 under visible light.

It can be observed in Fig. S4† that the morphology of the CuO/C_3N_4-2 had no obvious change after 5 cycles. In addition, the peak position in the XRD pattern had no significant deviation, suggesting that our samples had good stability. By comparing three CuO/C_3N_4 catalysts, it was found that the photocatalytic degradation performance of CuO/C_3N_4-2 was better than those of CuO/C_3N_4-1 and CuO/C_3N_4-3. This was due to the low CuO content of CuO/C_3N_4-1, resulting in the limited formation of heterojunctions. Moreover, the high CuO content of CuO/C_3N_4-3 caused the agglomeration of CuO on the surface of C_3N_4, leading to its low photocatalytic activity.

In addition to degradation efficiency, the ability to mineralize tetracycline is an important parameter to evaluate the production of highly toxic intermediate products and secondary pollution during the degradation process. TC samples degraded by CuO/C_3N_4-2 were collected every half an hour, and the mineralization rate and total organic carbon (TOC) removal rate were measured. After two hours, the mineralization rate of tetracycline approached 50%, and the total organic carbon content decreased by 30% (Fig. 6b). In contrast, the mineralization rates of some other catalytic materials for the photodegradation of tetracycline are given in Table S1.† These results confirmed that the catalyst exhibited not only excellent degradation efficiency, but also good mineralization ability to decompose tetracycline, ensuring the transformation of the pollutant into less harmful byproducts.

In order to explore the mechanism of photocatalytic degradation of heterojunctions formed by CuO and C_3N_4, the schematic diagram of band structure was composed, as shown in Fig. 6c. To obtain the carrier concentrations of C_3N_4 and CuO, the Mott–Schottky curves were tested at 1 kHz, as shown in Fig. S5.† The slopes of the curves are both positive, indicating that C_3N_4 and CuO are n-type semiconductors. According to the Mott–Schottky equation, the carrier concentrations of C_3N_4 and CuO were 3.07×10^{14} cm^{-3} and 7.36×10^{12} cm^{-3}, respectively. Based on the relationship between the carrier concentration and the Fermi level, such a carrier concentration caused the Fermi level of an n-type semiconductor to shift by about 0.1 eV towards the conduction band at room temperature.[40] As the Fermi level of C_3N_4 was higher than that of CuO, an interfacial charge transfer occurred after contact between C_3N_4 and CuO. Electrons drifted from C_3N_4 to CuO. As a result, the C_3N_4 side lost electrons with positive charges, and the CuO side obtained electrons with negative charges, forming an interfacial electric field (IEF) and causing the band to bend. This resulted in a typical n–n S-scheme heterojunction structure consisting of a reduction photocatalyst (C_3N_4) with a higher Fermi level and an oxidation photocatalyst (CuO) with a lower Fermi level. This promoted the transfer of electrons from the conduction band of CuO to the valence band of C_3N_4. Compared with a conventional type II heterojunction, an n–n S-scheme heterojunction structure not only ensures the separation of photogenerated carriers, but also maintains the high redox capacity of the catalyst. Therefore, CuO/C_3N_4 catalysts that form S-scheme heterojunctions show both good TC degradation performance and good TC mineralization ability.

4. Conclusions

In this study, we present a straightforward method to synthesize CuO/C_3N_4 S-scheme heterojunction photocatalysts for the effective degradation of tetracycline. This work combined the recycling of metal resources from solid waste with the preparation of photocatalysts. The S-scheme heterojunction was constructed by exploiting the Fermi level difference between CuO and C_3N_4. The formation of CuO/C_3N_4 S-scheme heterojunctions not only facilitated the separation and transportation of photogenerated charge carriers, but also inhibited their recombination, thereby enhancing the utilization of visible light by the catalyst and leading to an improved photocatalytic performance. After the formation of the S-scheme heterojunction, the carrier lifetime of the catalyst increased from 1.32 ns to 4 ns, approximately tripling the original charge mobility. Meanwhile, the formation of the S-scheme heterojunction also retained the strong redox ability of the catalyst, contributing to its effective degradation and mineralization performance in the tetracycline degradation. In comparison with pure C_3N_4, the photodegradation performance of tetracycline using CuO/C_3N_4 as the catalyst was significantly enhanced, achieving approximately a 50% mineralization rate and total organic carbon (TOC) removal of tetracycline in 2 hours. This research not only introduces a novel approach for the recovery of metallic elements from solid waste, but also demonstrates its effective utilization in the development of advanced photocatalysts.

Author contributions

Jiawen Liu performed the investigation, data curation and writing – original draft preparation. Jiahui Lin and Kai Yi

implemented the catalyst synthesis and characterization methods. Fangyan Liu and Feng Gao performed the investigation. Feng Huang contributed to project administration and funding acquisition. Mengye Wang performed writing – review and editing, supervision, project administration and funding acquisition.

Conflicts of interest

There are no conflicts to declare.

Acknowledgements

This study was financially supported by the National Natural Science Foundation of China (No. 21905317 and U23B20166), the Young Elite Scientists Sponsorship Program by CAST (2019QNRC001), and the Fundamental Research Funds for the Central Universities, Sun Yat-sen University (76180-31620007).

References

1 S. K. Loeb, P. J. J. Alvarez, J. A. Brame, E. L. Cates, W. Choi, J. Crittenden, D. D. Dionysiou, Q. Li, G. Li-Puma, X. Quan, D. L. Sedlak, T. David Waite, P. Westerhoff and J.-H. Kim, *Environ. Sci. Technol.*, 2018, **53**, 2937–2947.
2 M. Yuan, M. Gong, H. Huang, Y. Zhao, Y. Ying and S. Wang, *Inorg. Chem. Front.*, 2022, **9**, 5725–5734.
3 X. Guo, M. Duan, J. Zhang, B. Xi, M. Li, R. Yin, X. Zheng, Y. Liu, F. Cao, X. An and S. Xiong, *Adv. Funct. Mater.*, 2022, **32**, 2209397.
4 X. Guo, J. Zhang, L. Yuan, B. Xi, F. Gao, X. Zheng, R. Pan, L. Guo, X. An, T. Fan and S. Xiong, *Adv. Energy Mater.*, 2023, **13**, 2204376.
5 X. Guo, J. Shi, M. Li, J. Zhang, X. Zheng, Y. Liu, B. Xi, X. An, Z. Duan, Q. Fan, F. Gao and S. Xiong, *Angew. Chem., Int. Ed.*, 2023, **62**, e202314124.
6 C. Tian, J. Lv, W. Zhang, H. Wang, J. Chao, L. Chai and Z. Lin, *Angew. Chem., Int. Ed.*, 2022, **61**, e202206947.
7 C. Zhang, D. Qin, Y. Zhou, F. Qin, H. Wang, W. Wang, Y. Yang and G. Zeng, *Appl. Catal., B*, 2022, **303**, 120904.
8 M. Li, Y. Wu, E. Gu, W. Song and D. Zeng, *J. Alloys Compd.*, 2022, **914**, 165339.
9 J. Zhou, F. Pan, Q. Yao, Y. Zhu, H. Ma, J. Niu and J. Xie, *Appl. Catal., B*, 2022, **317**, 121811.
10 H. Zhang, F. Wan, X. Li, X. Chen, S. Xiong and B. Xi, *Adv. Funct. Mater.*, 2023, **33**, 2306340.
11 P. Li, S. Zhao, Y. Huang, Q. Huang, B. Xi, X. An and S. Xiong, *Adv. Energy Mater.*, 2023, **13**, 2303360.
12 C. Liu, L. Chen, D. Ding and T. Cai, *Appl. Catal., B*, 2019, **254**, 312–320.
13 W. Liu, F. Huang, Y. Liao, J. Zhang, G. Ren, Z. Zhuang, J. Zhen, Z. Lin and C. Wang, *Angew. Chem., Int. Ed.*, 2008, **47**, 5619–5622.
14 B. Han, X. Ou, Z. Deng, Y. Song, C. Tian, H. Deng, Y. J. Xu and Z. Lin, *Angew. Chem., Int. Ed.*, 2018, **57**, 16811–16815.
15 Z. Wu, M. Wang, Y. Bai, H. Song, J. Lv, X. Mo, X. Li and Z. Lin, *Chem. Eng. J.*, 2023, **464**, 142532.
16 W. Yu, T. Zhang and Z. Zhao, *Appl. Catal., B*, 2020, **278**, 119342.
17 Y. Zhang, Y. Li, X. Xin, Y. Wang, P. Guo, R. Wang, B. Wang, W. Huang, A. J. Sobrido and X. Li, *Nat. Energy*, 2023, **8**, 504–514.
18 B. Dai, C. Lu, J. Kou, Z. Xu and F. Wang, *J. Alloys Compd.*, 2017, **696**, 988–995.
19 S. Yao, J. Liu, F. Liu, B. Wang, Y. Ding, L. Li, C. Liu, F. Huang, J. Fang, Z. Lin and M. Wang, *Environ. Sci.: Nano*, 2022, **9**, 1996–2005.
20 C. Zhang, C. Xie, Y. Gao, X. Tao, C. Ding, F. Fan and H. L. Jiang, *Angew. Chem., Int. Ed.*, 2022, **61**, e202204108.
21 H. Yang, *Mater. Res. Bull.*, 2021, **142**, 111406.
22 J. Lu, X. Sun, Z. Chen, Y. Shen, H. Yuan, F. Guo and W. Shi, *Appl. Surf. Sci.*, 2024, **642**, 158648.
23 X. Q. Tan, S. F. Ng, A. R. Mohamed and W. J. Ong, *Carbon Energy*, 2022, **4**, 665–730.
24 L. Zhang, J. Zhang, H. Yu and J. Yu, *Adv. Mater.*, 2022, **34**, 2107668.
25 P. Zhou, Y. Wang, X. Yan, Y. Gan, C. Xia, Y. Xu and M. Xie, *Appl. Catal., B*, 2024, **343**, 123485.
26 Q. Xu, L. Zhang, B. Cheng, J. Fan and J. Yu, *Chem*, 2020, **6**, 1543–1559.
27 Q. Zhang, M. Sun, C.-Y. Yuan, Q.-W. Sun, B. Huang, H. Dong and Y.-W. Zhang, *ACS Catal.*, 2023, **13**, 7055–7066.
28 S. Yang, H. Li, H. Li, H. Li, W. Qi, Q. Zhang, J. Zhu, P. Zhao and L. Chen, *Appl. Catal., B*, 2022, **316**, 121612.
29 G. Z. S. Ling, S. F. Ng and W. J. Ong, *Adv. Funct. Mater.*, 2022, **32**, 2111875.
30 H. Chen, Y. Xing, S. Liu, Y. Liang, J. Fu, L. Wang and W. Wang, *Chem. Eng. J.*, 2023, **462**, 142038.
31 X. Wu, R. Zhong, X. Lv, Z. Hu, D. Xia, C. Li, B. Song and S. Liu, *Appl. Catal., B*, 2023, **330**, 122666.
32 X. Zhang, P. Ma, C. Wang, L. Gan, X. Chen, P. Zhang, Y. Wang, H. Li, L. Wang, X. Zhou and K. Zheng, *Energy Environ. Sci.*, 2022, **15**, 830–842.
33 X. Zhang, X. Yuan, L. Jiang, J. Zhang, H. Yu, H. Wang and G. Zeng, *Chem. Eng. J.*, 2020, **390**, 124475.
34 Y. Yang, X. Li, C. Zhou, W. Xiong, G. Zeng, D. Huang, C. Zhang, W. Wang, B. Song, X. Tang, X. Li and H. Guo, *Water Res.*, 2020, **184**, 116200.
35 L. Zhang and Z. Xu, *J. Cleaner Prod.*, 2016, **127**, 19–36.
36 H. Song, X. Ou, B. Han, H. Deng, W. Zhang, C. Tian, C. Cai, A. Lu, Z. Lin and L. Chai, *Angew. Chem., Int. Ed.*, 2021, **60**, 24054–24058.
37 B. Han, X. Ou, Z. Zhong, S. Liang, X. Yan, H. Deng and Z. Lin, *Appl. Catal., B*, 2021, **283**, 119594.
38 F. Wei, Y. Liu, H. Zhao, X. Ren, J. Liu, T. Hasan, L. Chen, Y. Li and B. Su, *Nanoscale*, 2018, **10**, 4515–4522.
39 Z. Huang, J. Song, L. Pan, Z. Wang, X. Zhang, J. Zou, W. Mi, X. Zhang and L. Wang, *Nano Energy*, 2017, **40**, 308–316.
40 D. A. Neamen, *Semiconductor Physics and Devices: Basic Principles*, 3rd edn, 2012.

